New Journal of Physics
The open-access journal for physics

Imaging with polarized neutrons

Martin Dawson[1], **Ingo Manke**[1,2,4], **Nikolay Kardjilov**[1], **André Hilger**[1], **Markus Strobl**[1,3] **and John Banhart**[1,2]

[1] Helmholtz Centre Berlin for Materials and Energy, Germany
[2] Technische Universität Berlin, Germany
[3] Universität Heidelberg, Germany
E-mail: manke@helmholtz-berlin.de

New Journal of Physics **11** (2009) 043013 (19pp)
Received 16 September 2008
Published 7 April 2009
Online at http://www.njp.org/
doi:10.1088/1367-2630/11/4/043013

Abstract. Neutrons have zero net electrical charge and can thus penetrate deeply into matter, but their intrinsic magnetic moment makes them highly sensitive to magnetic fields. These properties have been combined with radiographic (2D) and tomographic (3D) imaging methods to provide a unique technique to probe macroscopic magnetic phenomena both within and around bulk matter. Based on the spin-rotation of a polarized neutron beam as it passes through a magnetic field, this method allows the direct, real-space visualization of magnetic field distributions. It has been used to investigate the Meissner effect in a type I (Pb) and a type II (YBCO) superconductor, flux trapping in a type I (Pb) superconductor, and the electromagnetic field associated with a direct current flowing in a solenoid. The latter results have been compared to predictions calculated using the Biot–Savart law and have been found to agree well.

[4] Author to whom any correspondence should be addressed.

Contents

1. Introduction

Neutron imaging has proven to be successful across a broad spectrum of scientific disciplines and industrial applications [1]–[11], providing important complementary information to that given by x-rays. Their zero net electrical charge allows them to penetrate thick layers of many materials, yet they are sensitive to several light elements (e.g. hydrogen, boron and lithium), and are also able to differentiate isotopes of the same element. Neutrons are also highly sensitive to magnetic fields, a property that makes them useful for investigating magnetic phenomena. Conventionally, such studies have been limited either to material surfaces and the surrounding free space (e.g. neutron reflectometry [12] and magneto-optical effects [13]–[15]), or to bulk magnetism (e.g. neutron spin echo, diffraction and interferometry [16]–[19]). However, recent experimental developments at the Helmholtz Centre Berlin for Materials and Energy (formerly the Hahn-Meitner Institute) in Germany have yielded an imaging technique that uses the magnetic interaction of spin-polarized neutrons to visualize magnetic field distributions both in free space and within the bulk of massive samples [20]–[23].

2. Principles of polarized neutron imaging

The neutron's sensitivity to magnetic fields lies in its intrinsic magnetic moment, $\vec{\mu}$ ($-9.66 \times 10^{-27}\,\mathrm{J\,T^{-1}}$); the '–' indicates that the moment is always aligned anti-parallel to its associated spin, which has a quantum number $s = 1/2$. Under the influence of an applied magnetic field, $\vec{B}$, the time-dependent behavior of the spin vector, $\vec{S}$, can be completely described by the Schrödinger wave equation

$$\frac{\mathrm{d}}{\mathrm{d}t}\vec{S} = \gamma\left[\vec{S}(t) \times \vec{B}(t)\right], \tag{1}$$

where γ is the gyromagnetic ratio of the neutron ($-1.832 \times 10^{8}\,\mathrm{rad\,s^{-1}\,T^{-1}}$).

Within a field, Zeeman splitting means that there are only two possible neutron spin orientations: parallel (spin-up), and anti-parallel (spin-down), i.e. the field acts as a quantization or polarization axis. The scalar polarization, P, is quantified as

$$P = \frac{N(\uparrow) - N(\downarrow)}{N(\uparrow) + N(\downarrow)}, \tag{2}$$

where $N(\uparrow)$ is the number of spin-up neutrons and $N(\downarrow)$ is the number of spin-down neutrons.

This can be expressed in vector form, $\vec{P}$, as the average over all spin-states for the whole beam normalized to the modulus

$$\vec{P} = \frac{\left\langle \vec{S} \right\rangle}{1/2} = 2\left\langle \vec{S} \right\rangle. \tag{3}$$

It can be shown that this polarization vector behaves exactly like a classical magnetic moment [24]. In an applied magnetic field a moment experiences a torque

$$\vec{\Gamma} = \vec{\mu} \times \vec{B} \tag{4}$$

causing it to undergo Larmor precession around the field with a frequency, ω, given by

$$\omega = \gamma B, \tag{5}$$

where B is the scalar magnitude of the magnetic field. For a neutron traveling along a path, s, with a velocity, v, the total precession angle, $\mathrm{d}\theta$, is

$$\mathrm{d}\theta = \omega \frac{\mathrm{d}s}{v}, \tag{6}$$

which can be expressed in terms of the neutron wavelength, λ, as

$$\mathrm{d}\theta = \frac{\gamma \lambda m}{h} \int B \, \mathrm{d}s, \tag{7}$$

where m is the neutron rest mass (1.675×10^{-27} kg) and h is Planck's constant (6.626×10^{-34} J s^{-1}).

Changes in the orientation of the moment are thus indicative of the underlying magnetic field distribution it traverses. This can be measured using a polarized neutron beam (one in which only one spin-state is populated) and analyzing the cumulated precession angle of the polarization vector. If the field component perpendicular to the polarization vector is negligible, then the polarization will be preserved. If, however, the field component perpendicular to the polarization vector is significant, then the vector will rotate, beating between states (figure 1).

Polarization analysis can be combined with standard imaging methods to visualize spatial variations in the cumulated spin precession angle.

3. CONRAD at the Helmholtz Centre Berlin

Experiments were performed on the cold neutron radiography and tomography station (CONRAD) at the Helmholtz Centre Berlin for Materials and Energy (figure 2). CONRAD is positioned at the end of a curved, nickel-coated neutron guide (cross section 3×12 cm^2), which faces the cold source of the 10 MW Hahn–Meitner reactor and receives neutrons with an energy spectrum in the range 2–10 Å (peaking at ~3.1 Å) [25]. The instrument parameters are given in table 1.

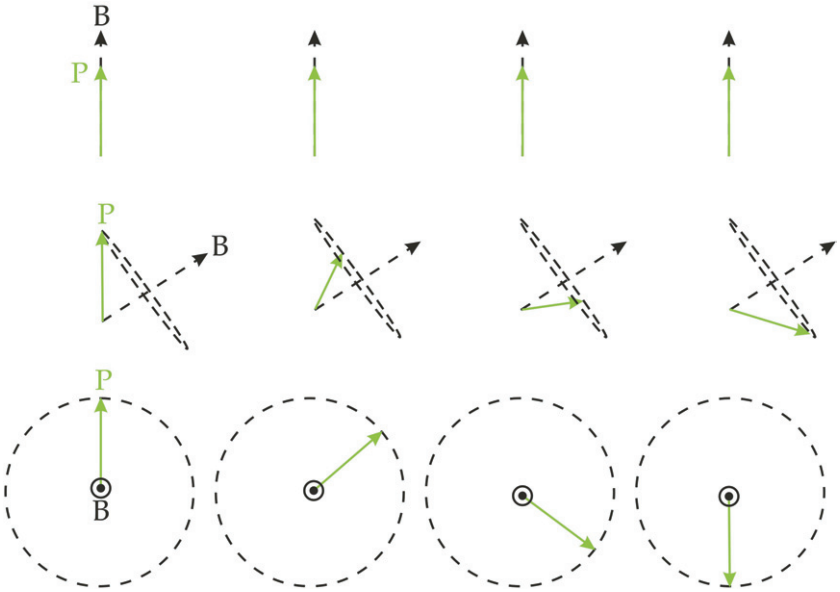

Figure 1. The orientation of the polarization axis will be preserved if it is parallel to an applied magnetic field (top), but will precess (and flip) if there is a significant perpendicular magnetic field component.

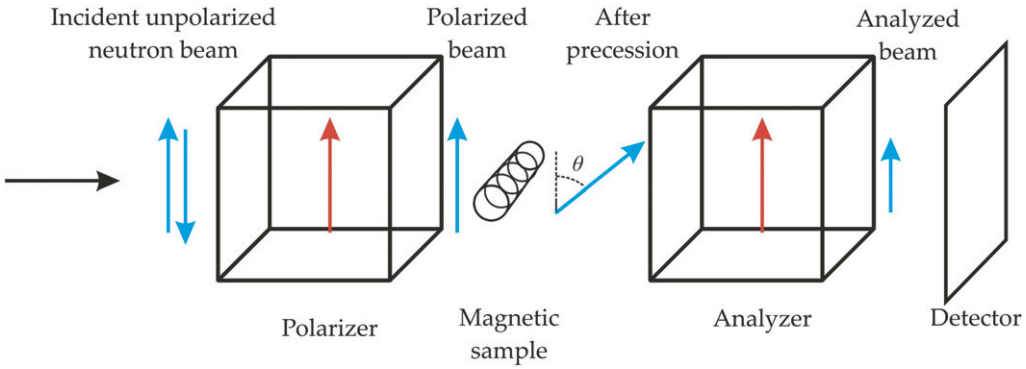

Figure 2. A schematic diagram of the experimental setup used for polarized neutron imaging on CONRAD.

The experimental setup (figure 2) used two spin filters (see below): one placed upstream of the sample to polarize the incident beam, and one placed downstream of the sample to analyze the polarization of the resulting beam. The beam intensity was then measured by a position sensitive detector system based on a lithium fluoride scintillator positioned in the plane perpendicular to the beam propagation direction. This layer converted the neutrons to visible light (565 nm), which was reflected by 90° by a mirror and focused onto the chip of a cooled, 16-bit Andor DW436N-BV CCD camera (2048 × 2048 pixels).

The key to the image formed is that the analyzer only transmits the component of the beam polarization that is parallel to its own polarization axis. As a result, the beam intensity measured behind the analyzer is the incident intensity modulated both by attenuation (the magnitude of

Table 1. Instrumental parameters of the two imaging positions available on CONRAD.

	L/D	Typical spatial resolution (μm)	Max. neutron flux at sample (n cm^{-2}s^{-1})	Typical exposure times (s)	Typical beam size (cm^2)
Position I	70	300–500	$\sim 2 \times 10^8$	0.01–0.5	3×12
Position II					
3 cm aperture	167	200–400	$\sim 2.0 \times 10^7$	1–5	12×12
2 cm aperture	250	100–200	$\sim 1.0 \times 10^7$	5–15	11×11
1 cm aperture	500	50–100	$\sim 2.5 \times 10^6$	10–5	10×10

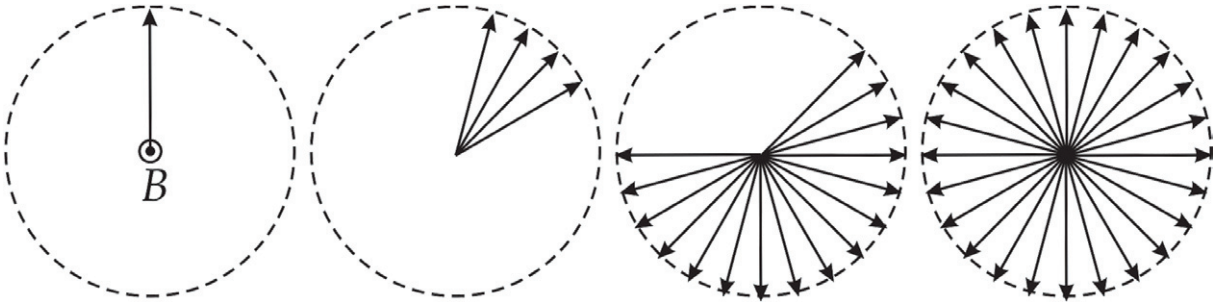

Figure 3. Precession will cause a polychromatic neutron beam to dephase and depolarize in the plane perpendicular to the field. The arrows indicate the vector polarization for neutrons of different wavelengths, with time increasing from left to right.

which can be found from a standard radiograph) and by a sinusoidal function that is directly related to the precession angle of the polarization vector. With the polarizer and analyzer aligned parallel, this can be approximated as

$$I(x, y) = I_0(x, y) \underbrace{\exp\left[-\int \alpha(s)\, \mathrm{d}s\right]}_{\text{attenuation}} \underbrace{\frac{1}{2}(1 + \cos\theta\ (x, y))}_{\text{precession}}, \tag{8}$$

where I is the measured intensity, I_0 is the incident intensity at the sample position, α is the spatially dependent linear attenuation coefficient of the sample, and s is the path length through the sample [20]. In terms of precession, the maximum (minimum) intensity will be measured when the beam polarization and the analyzer are aligned perfectly parallel (anti-parallel).

From (7), the total precession angle (though not the rate of precession) is dependent on the neutron wavelength and it is therefore necessary to use a monochromatic beam; a polychromatic beam would dephase upon precession, resulting in a loss of polarization (figure 3). The beam was monochromated via double reflection from a pair of pyrolytic graphite crystals (PGC) with a mosaicity of 3° [26]. The adjustable positioning and angling of the PGCs ensured that the beam propagation direction was unperturbed and allowed the selection of wavelengths in the range 2.0–6.0 Å ($\Delta\lambda/\lambda = 0.12$). The wavelength selection decreases the beam intensity to ~1% of that of the polychromatic beam, which still allows single radiographs to be recorded within several minutes.

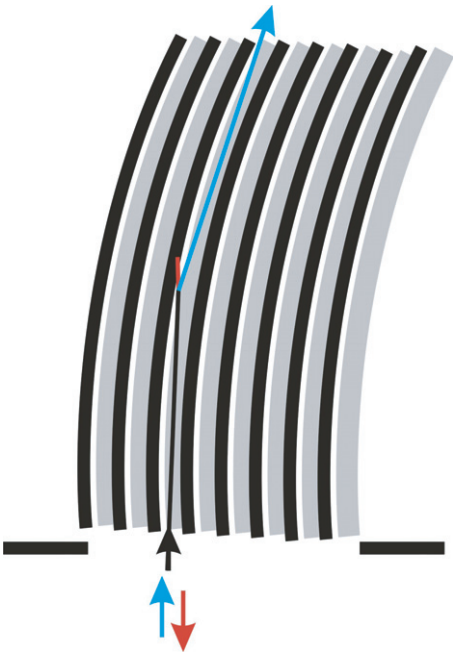

Figure 4. A diagram of a bender that is magnetized such that the spin-up (blue) component of the beam is reflected from the supermirror surface (white) along the path of the silicon (gray). The spin-down (red) component passes through the supermirror and is absorbed by the gadolinium (black). A cadmium screen (black, horizontal) limits the beam to the field of view of the bender.

4. Spin filters

The spin filters were constructed from a stack of 100 bent single-crystal silicon wafers measuring $75 \times 50 \times 0.25$ mm. The surface on the outer curve of each wafer was coated with an iron–cobalt–silicon supermirror ($m = 2$), whereas the inner surface was coated with 600 nm of gadolinium [27, 28].

Two permanent ferromagnets were used to magnetize the supermirror layers, thus making their refractive index, n, neutron spin-dependent

$$n_{\pm} = 1 - \left(\frac{N\lambda^2}{2\pi}\right)\left(\vec{b} \pm \vec{p}\right), \tag{9}$$

for neutrons with spin parallel (+) or anti-parallel (–) to the magnetization direction, where N is the density of scattering atoms, λ the neutron wavelength, b the mean coherent nuclear scattering length, and p the magnetic scattering length. This yields two critical angles (from Snell's law), θ_c, for total external reflection given by

$$\theta_{c_{\pm}} = \lambda\left[\frac{N}{\pi}\left(\vec{b} \pm \vec{p}\right)\right]^{1/2}, \tag{10}$$

between which the reflected beam is completely polarized. For $\lambda = 3.0$ Å, $\theta_{c+} = 0.3^{\circ}$. By correctly aligning the bender, one neutron spin-state (the spin-up neutrons) were preferentially reflected and 'bent' along the path of the wafers towards the detector (figure 4). The spin-down

Figure 5. A radiograph showing the vertical striping inhomogeneities produced by the structure of a bender. The field of view is 1.5×4.5 cm.

neutrons passed through the supermirror and were absorbed by the gadolinium layer (i.e. there was no straight-through beam). The typical polarization achieved with such a bender is 95%.

A cadmium screen with a window 1×4 cm was placed in front of each bender (polarizer and analyzer) in order to prevent neutrons that had not passed through both benders from reaching the detector. Objects larger than this window could still be imaged by scanning the sample and recombining images from multiple positions.

Some disadvantages of using benders are that beam attenuation caused by their physical structure produces vertical striping inhomogeneities in the beam intensity profile (figure 5), and the polarization produced is non-uniform across the beam (the beam polarization received by neighboring pixels can vary by 5%). These factors can be corrected (by normalization), but they have an impact on the potential quality of the data and create inaccuracies in the recombined images of larger samples.

5. Limitations

The experimental arrangement outlined above has some limitations. First of all, it can only be applied reliably to magnetic fields below a certain strength, as the beam's imperfect monochromaticity means that multiple precessions in regions where the field is too strong will lead to multiple, non-distinguishable rotations and, eventually, dephasing. If the neutrons dephase completely then the beam will no longer be polarized and it will not be possible to resolve any magnetic effects. The problem of dephasing could be overcome by improving the beam monochromaticity or using a spin-echo setup [29] to counteract the multiple precessions.

Secondly, the uniaxial polarization analysis means that measurement of the exact vector field distribution is not straight forward, since only the scalar polarization is measured. Information about the polarization vector in the plane perpendicular to the polarization axis

is lost; in general, a precession of ϕ is indistinguishable from a rotation of $n\pi \pm \phi$ ($n = 2, 4, 6, \ldots$) around the same axis. In order to recover the three-dimensional (3D) vector polarization, it is necessary to measure the scalar polarization in three mutually orthogonal directions, e.g. by using spin flippers. However, a complex 3D vector field will produce a spin rotation that cannot be easily correlated to the vector field from which it originated (see below).

It should be noted that the limitation of field strength with respect to multiple precessions and dephasing depends on both the field strength and the length of the path (cf (7)); as the path length is reduced, stronger fields can be tolerated. For a polarized monochromatic beam with $\Delta\lambda/\lambda = 0.1$ traversing a uniform field-oriented perpendicular to the beam propagation direction, after ten complete precessions the spins of the lowest energy neutrons will be 2π out of phase with those of the highest energy neutrons (i.e. the beam would be unpolarized). For a path length of 1 cm, this would occur for a field of $\sim$50 mT.

Finally, the experimental setup includes an inherent short-coming in that, for parallel beam geometry with a finite beam divergence, the best spatial resolution is attained with a minimum distance between the sample and the detector. Clearly, the necessity for the analyzer between the sample and the detector increases the separation. This is compounded by the fact that, when imaging samples that have/require strong magnetic fields, the sample–analyzer distance must be increased further in order to limit the effect of the field on the working of the analyzer. The increased separation leads to a reduction in spatial resolution and losses in the image quality.

6. Data processing/reference images

6.1. Separation of attenuation and spin rotation contrast

Radiographic images require normalization to a reference image in order to correct for instrumental inhomogeneities (e.g. in the intensity profile across the beam). The reference is usually an open beam image (i.e. one in which no sample is present), but for polarized neutron imaging it is sometimes more useful to use an image of the sample in the absence of any magnetic field, i.e. by switching the field off (in the case of electromagnetic or externally applied fields). Since attenuation and spin rotation are mutually independent (cf (8)), such a reference image allows them to be separated from one another; both beam inhomogeneities and sample attenuation are normalized, resulting in an image that contains only magnetic effects. This is particularly useful when attenuation is the dominant effect and subtle magnetic effects would otherwise be overwhelmed. Note that this method is not possible if the magnetic field cannot be switched off (naturally magnetized materials for example); in such cases, the reference image is an image containing the polarizer and analyzer (this corrects for inherent beam inhomogeneities and inhomogeneities introduced by the polarization equipment).

This is demonstrated in figure 6, which shows a pellet of $YBa_2Cu_3O_7$ (YBCO), a type II superconductor, cooled below its critical temperature ($T_c = 90$ K) in the presence of a homogeneous 0.1 mT field. As a consequence of the Meissner effect, the magnetic field is expelled in the superconducting state (see figure 6(a)). Due to neutron absorption in the pellet, it is difficult to differentiate between attenuation and magnetic signals in the raw images measured at 100 and 20 K (figure 6(b)). However, normalization of these images to an image measured at 100 K in the absence of an applied magnetic field allows the magnetic signal to be viewed independently (figure 6(c)). At 100 K the magnetic field is distributed homogeneously (the signal in the image is uniform). At 20 K strong inhomogeneities caused by the expulsion of

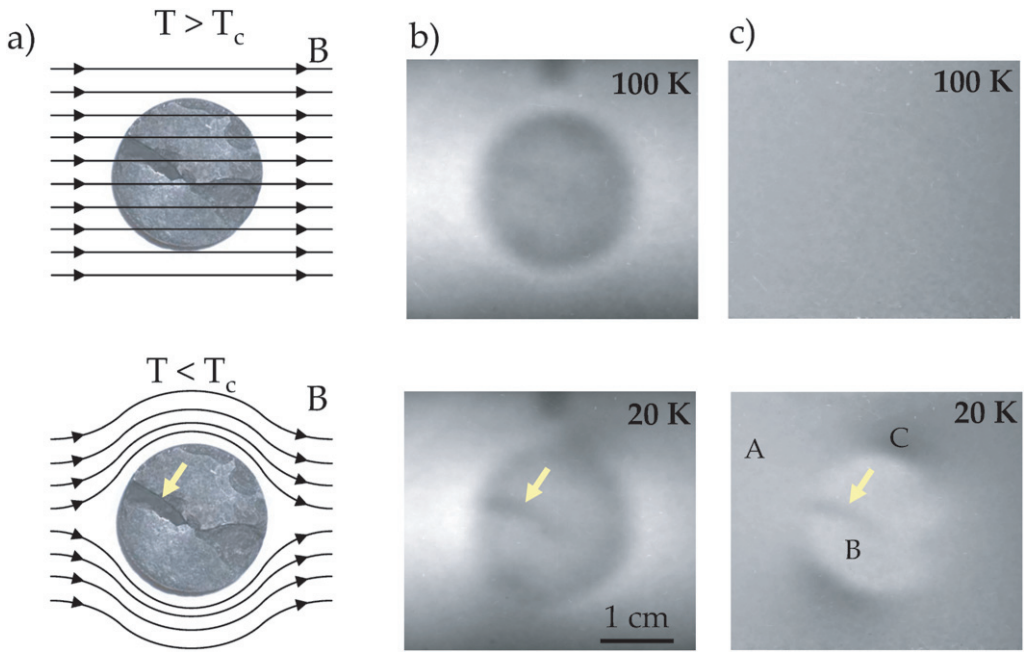

Figure 6. Images of the field associated with the Meissner effect in a superconducting YBCO pellet (Ø2 cm) above and below the critical temperature ($T_c = 90$ K), showing (a) schematic diagrams, (b) raw (unnormalized) radiographs, and (c) radiographs normalized to a reference image. The reference was an image of the sample in zero field at 100 K. The arrow indicates a region where expulsion of the field is incomplete.

the field from the pellet can be seen. Three regions can be distinguished. For neutrons passing through the unperturbed field, the precession angle remains constant; the measured intensity here is uniform (A in figure 6). For neutrons passing through the pellet, the field is reduced and the precession angle is smaller than in the unperturbed region; the measured intensity here is higher than in the unperturbed region (cf (8)) (B in figure 6). For neutrons passing through the regions of stronger magnetic field (above and below the pellet in figure 6(a)), the precession angle is larger than in the unperturbed region; the measured intensity here is lower than in the unperturbed region (cf (8)) (C in figure 6). The latter point applies also to a defect running across the pellet in which some of the expelled magnetic field becomes trapped.

6.2. Spin flipping

The contrast of the magnetic field in an image can be switched by using (for example) a spin flipper to rotate the beam polarization incident at the sample position by π, this is equivalent to the polarization and analysis axes being aligned anti-parallel. In this case, the intensity measured behind the analyzer is given approximately by

$$I(x, y) = I_0(x, y) \underbrace{\exp\left[-\int \alpha(s)\, \mathrm{d}s\right]}_{\text{attenuation}} \underbrace{\frac{1}{2}(1 - \cos\theta\ (x, y))}_{\text{precession}} \tag{11}$$

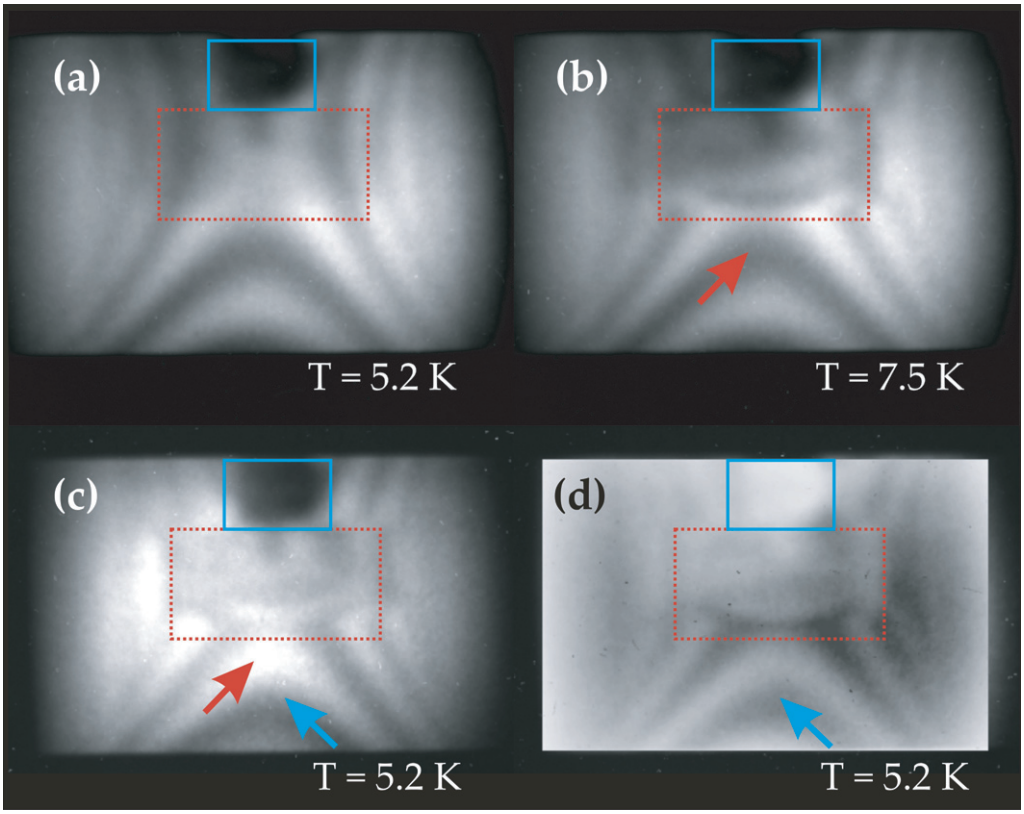

Figure 7. Radiographs of the magnetic field associated with the Meissner effect in a superconducting lead cylinder ($T_c = 7.2$ K), $\emptyset 1 \times 3$ cm, showing the situation (a) and (b) with, and (c) without a π-flipper positioned between the polarizer and the sample. As a comparison, (d) is the negative image of (b). The red, dashed/blue, solid box indicates the approximate position of the lead cylinder/the steel fixture holding the cylinder in place. The arrows indicate equivalent positions and are intended as a guide to the eye.

(cf (8)). This is demonstrated in figure 7, which shows the magnetic field distribution inside and around a lead cylinder, a type I superconductor ($T_c = 7.2$ K) (cf figures 9, 11 and 12). A homogeneous 10 mT magnetic field was applied parallel to the cylinder axis and perpendicular to the beam polarization axis and images were recorded above and below the critical temperature. Above T_c the field permeates the lead (figure 7(a)), but below T_c the field is largely expelled (figure 7(b)) due to the Meissner effect, resulting in disturbances in the field in the vicinity of the cylinder.

Figure 7(c) is measured with the same arrangement as figure 7(b), but with the beam polarization flipped by π before interaction with the sample. The image recorded without the π-flip is approximately the negative of that recorded with the π-flip (i.e. dark becomes bright and vice versa, see red arrows). However, the regions in figure 7(b) where attenuation is dominant remain constant (i.e. the steel fixture holding the sample in place is dark in both cases (blue solid box)). For comparison, an actual negative image of figure 7(a) is shown in figure 7(d). In regions where magnetic effects dominate (i.e. in free space and inside the lead)

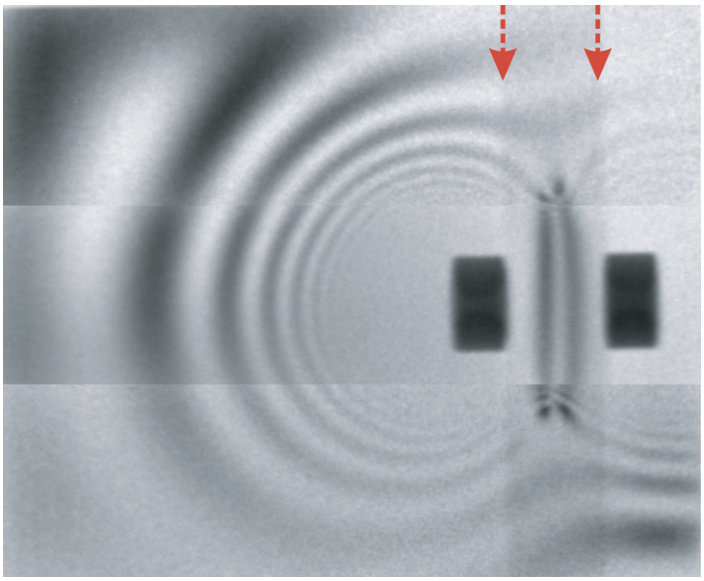

Figure 8. Radiograph of the magnetic field surrounding a pair of ring-shaped dipole magnets, oriented horizontally in the plane of the paper, separated by a sheet of aluminum (edges indicated by arrows.). The field of view is 13.8 × 11.3 cm and is a composite of images measured at three different positions. ([20], supplementary information.)

figures 7(c) and 8(d) correspond very well (blue arrows), but the contrast is switched in regions where attenuation dominates.

7. Results/radiography

The utility of this technique has already been demonstrated with a variety of magnetic systems. Figure 8 shows a radiographic image of a pair of ring-shaped magnets (the dipoles are oriented horizontally in the plane of the paper) separated by a piece of aluminum. The magnetic field is visible both in free space and within the bulk of the aluminum spacer (arrows). The strength of the magnetic field around the magnet diminishes (approximately) with the inverse of the square of the distance from the magnets. As a result, the magnitude of the total neutron precession also declines, resulting in a series of maxima and minima in intensity, whose period increases with distance (cf (8)). The image shown is approximately 13.8 × 11.3 cm and is a composite of images measured at three different positions (due to the limited field of view of the benders). Imperfect screening of the magnetic sample meant that the magnetic field interfered with the polarizing properties of the analyzing bender. Thus, as the relative positions of the sample and analyzer were adjusted for each image, the measured polarization changed also. Consequently, the three individual images do not align exactly.

Figure 9 shows an investigation of so-called trapped flux in the polycrystalline lead cylinder shown in figure 8 [13, 30]. Upon switching off the magnetic field below the critical temperature, it can bee seen that the magnetic field is not completely expelled—some remains trapped inside the lead due to grain boundaries (as well as other lattice defects, impurities, etc). As the temperature is then increased, the trapped field gradually disperses until, above T_c, where

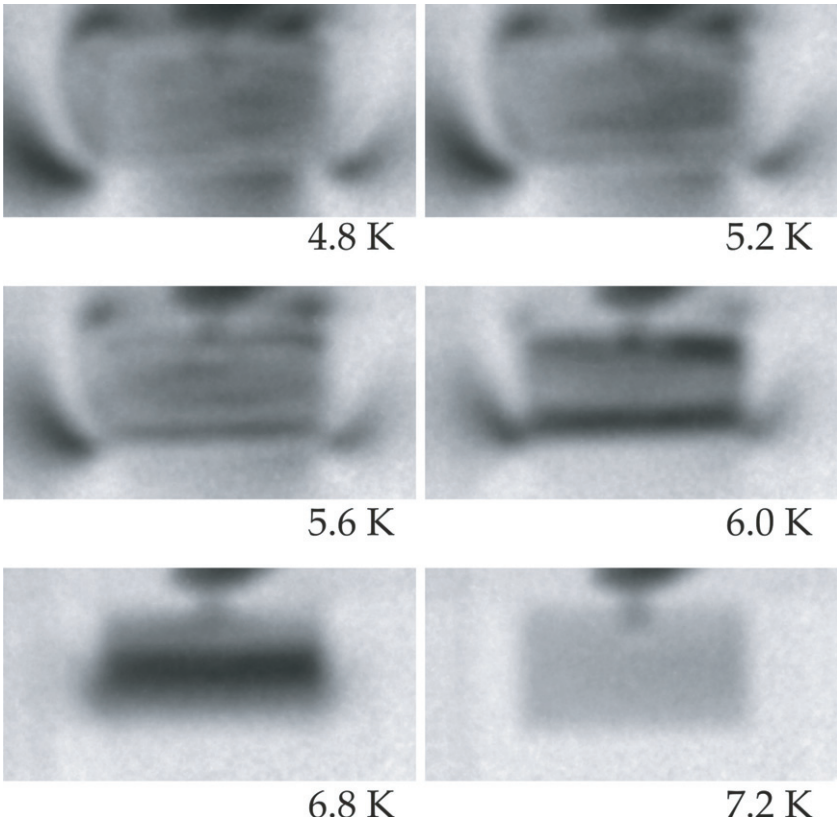

Figure 9. Radiographs of the magnetic field associated with trapped flux in a lead cylinder ($T_c = 7.2$ K), showing the dispersal trapped field as the temperature rises.

the lead is no longer superconducting, the field is no longer evident (cf the image at 7.2 K, which shows only attenuation).

8. Extension into three dimensions/tomography

This technique is not limited to two dimensions. Since the neutrons penetrate the sample it is possible to use this technique to view a sample from any viewpoint simply by rotating it, thereby revealing detailed information about the 3D magnetic field distribution.

However, there is currently no general method for tomographic reconstruction. The difficulty stems from the fact that different field distributions can produce identical total precession angles (zero field and a homogeneous field oriented parallel to the beam polarization axis would result in zero precession). An important facet to this problem is the aforementioned problem of only being able to determine unique precession angles smaller than π (larger angles can be resolved in some cases through comparison to calculated data, see below). While attenuation will always causes the beam intensity measured behind the analyzer to decrease, precession will cause it to periodically decrease and increase (see above), making it difficult to assign absolute values of the field strength along the flight path of the beam. Further, since the interaction is dependent on the relative orientation of the beam polarization axis to the magnetic field components it encounters, the ordering of the interactions (the magnetic field distribution

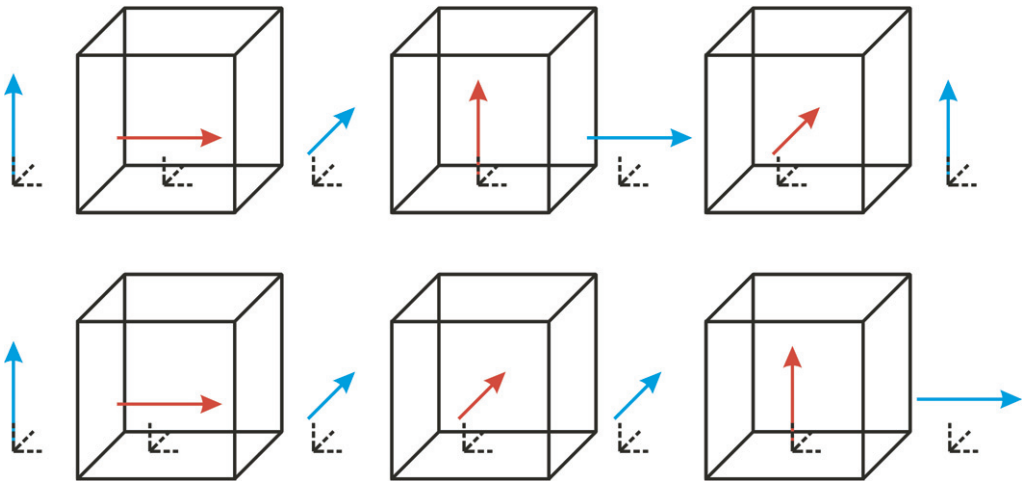

Figure 10. Diagram showing how the order in which a polarized neutron beam (blue) interacts with three mutually orthogonal magnetic fields (red) is nontrivial.

along a given trajectory) is nontrivial with respect to the cumulative precession angle. This is illustrated in figure 10. Attempts have been made [31]–[36] to formulate new algorithms to remedy this situation, but these have not yet come to fruition.

Figure 11 shows a series of radiographs of magnetic field trapped within a lead cylinder (cf figures 7, 9 and 12) at a temperature of 4.8 K as it is rotated around a vertical axis. In this case, the field is strong and extends beyond the bounds of the matter. Due to the strength (and complexity) of the field it is not possible to accurately correlate the final beam polarization (that measured in the images) with the magnetic field distribution that lead to that polarization. The darkest regions correspond to paths along which the neutrons' resultant precession angle is equal to π (i.e. a rotation from spin-up to spin-down). Though the initial and final polarization states are known, what are not clear are the steps in between. It is these steps that are required to resolve completely the magnetic field in three dimensions.

Nonetheless, in simple cases involving weak fields (i.e. precession angles smaller than π) oriented only (or mainly) perpendicularly to the beam polarization axis it is possible to make an ad hoc reconstruction [20] using standard tomography algorithms [30, 37]. Though this reconstruction will not be a complete representation of the exact magnetic field's vector form, it can reveal the 3D position of regions of higher magnetic field strength within a region of weak field. Figure 12 shows an example of a reconstruction for a weak trapped magnetic field inside a lead cylinder (cf figures 7 and 9) at a temperature of 7 K. Within the regions of trapped flux, the magnetic field strength is $\sim$0.5 mT, rising to 1.0 ± 0.2 mT at the center—small enough that the conditions for a tomographic reconstruction mentioned above are fulfilled. The tomographic reconstruction was calculated from 61 equally spaced projections recorded as the cylinder was rotated by 180° around a vertical axis and normalized to the open beam.

9. Comparison between experiment and calculation

In relatively simple cases, where the magnetic field distribution of the sample is either well-known (e.g. a permanent dipole magnet) or calculable (e.g. via the laws of electromagnetism), it

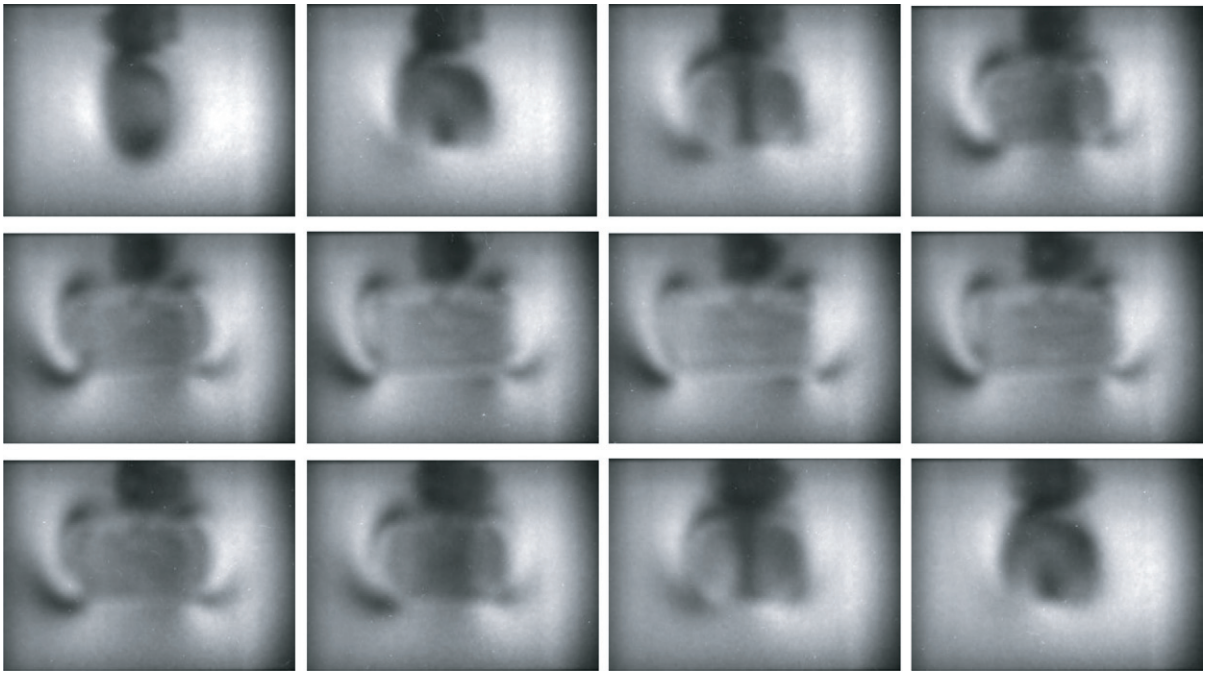

Figure 11. A series of radiographs of trapped flux in a lead cylinder as it is rotated around a vertical axis.

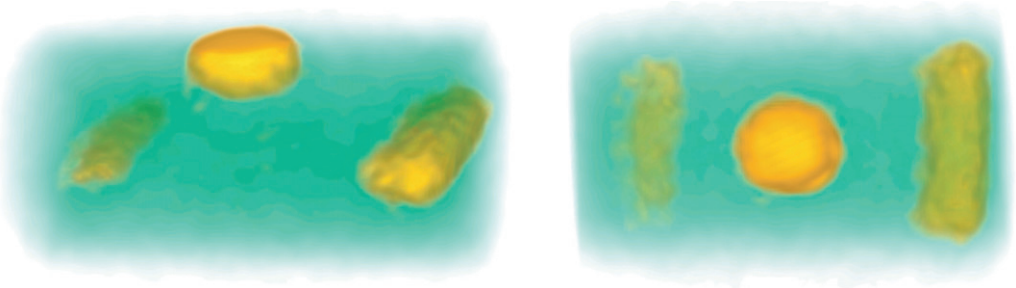

Figure 12. A standard back-projection reconstruction, revealing the 3D distribution of the trapped flux inside a superconducting lead cylinder [20].

is possible to compare the experimentally measured precession angle to calculation predictions. In the case of a well-known electrical current distribution flowing through a wire, the electromagnetically induced field can be calculated from the Biot–Savart law

$$\mathrm{d}\vec{B} = \frac{\mu_0}{4\pi} \frac{I\,\mathrm{d}\vec{L} \times \widehat{r}}{r^2}, \tag{12}$$

where $\vec{B}$ is the field vector, μ_0 is the permeability of free space ($4\pi \times 10^{-7}\,\mathrm{H\,m^{-1}}$), I is the current flowing in the wire, $\mathrm{d}\vec{L}$ is an infinitesimal vector length of the wire pointing in the direction of conventional current, and $\widehat{r}$ and r are a unit vector and the distance, respectively, from the wire to the point where the field is to be calculated. From (7), the overall local spin

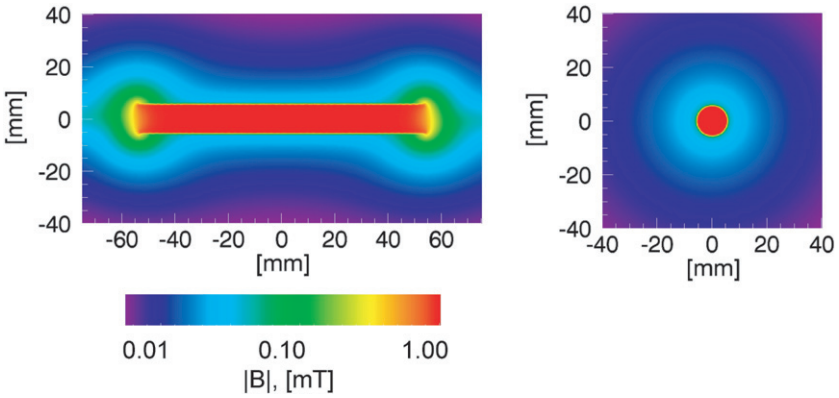

Figure 13. Longitudinal (left) and transverse (right) cross sections of the calculation of the field magnitude for a cylindrical solenoid (Ø10 × 100 mm, 88 windings) conducting a direct current of 1 A.

rotation at a given point is then given by

$$\theta = \frac{\gamma \lambda m}{h} \int \int \frac{\mu_0}{4\pi} \frac{I \mathrm{d}\vec{L} \times \hat{r}}{r^2} \mathrm{d}s. \tag{13}$$

Once the field distribution of the system is known, this can be used to computationally construct a 3D magnetic field matrix, with each element representing the magnetic field vector for a unit volume (a voxel). Neutrons with a defined polarization vector enter the first voxel and precess for a given time (depending on the neutron velocity), giving a new polarization vector, which is then passed to the next voxel along the trajectory of the neutron. Once the neutrons have passed through the matrix the total angle of precession can be used together with (8) to find the intensity measured in the calculated image.

Figure 13 shows the magnitude of the field calculated for a cylindrical solenoid of 88 windings with a diameter of 10 mm and a length of 100 mm conducting a direct current of 1 A. The field inside the solenoid (red regions) is homogeneous and is much stronger than the field at any point outside the solenoid.

Figure 14 shows the experimentally measured and calculated field around a pair of small solenoids with rectangular cross section, separated by 20 mm and supported on an aluminum rod as the direct current passing through them was varied. The coils were approximately identical with a length of 24.4 mm, a height of 7.5 mm, a depth of 21.5 mm, and 30 windings. In general the calculated and experimental results agree very well, though some deviations can be seen. These discrepancies occur because the calculations represent an idealized system where the coils are identical, perfectly aligned and self-contained, and isolated from external influences. Conversely, the coils used in the experiments suffer from irregularities introduced during their manufacture (red arrows in figure 14) and differences in the measured intensity (between experiment and calculation) can be seen in the vicinity of these points.

It is believed that the reconstruction in figure 12 works well because the cylindrical regions of trapped flux behave similarly to the electromagnetic solenoid in figure 13, i.e. the field is homogeneous within a small confined region outside of which the field is much weaker. For the same reason, the magnetic field surrounding the trapped flux in the lead cylinder in figure 11 also has a similar distribution to that surrounding the coils in figure 14.

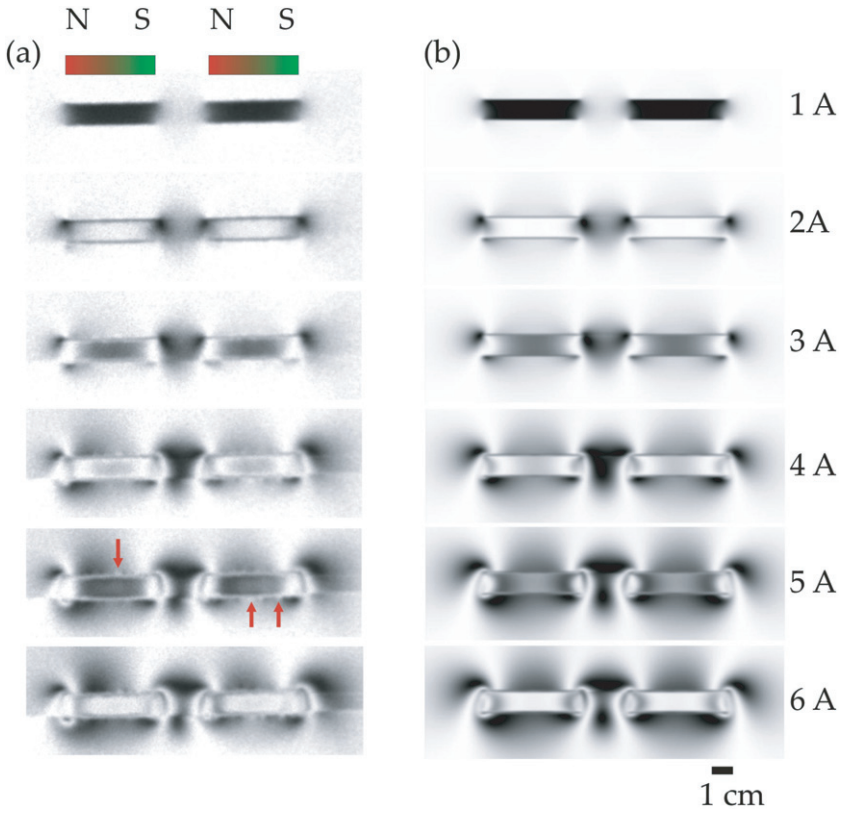

Figure 14. Visualization of (a) experimentally measured and (b) calculated radiographs of the magnetic field around a co-axial pair of small, rectangular solenoids ($24.4 \times 7.5 \times 21.5$ mm, 30 windings). The arrows indicate some of the anomalies caused by imperfections in the manufacture of the solenoids. ([20], supplementary information.)

The spatial resolution of the calculated results is limited only by the size of the individual voxels in the calculation, whereas the spatial resolution of the experiments—300 μm in the vertical direction and 500 μm in the horizontal direction—is limited by the divergence of the beam (particularly with regards to the sample–detector distance of 50 cm) and the finite resolution of the detector. This can be approximated in the calculated data by convolution with a blur function: an asymmetrical Gaussian with a full-width at half-maximum corresponding to the measured resolution in the vertical and horizontal directions.

This is illustrated in figure 15, which shows the magnetic field surrounding a small dipole magnet levitating above an YBCO pellet as a result of the Meissner effect. Convolution of the calculated data with the blur function causes fine-detail information to be lost and this result compares well with the experimental result. The artefact at the center of the calculated result is caused by the finite size of the voxels in the calculation. Due to the fact that the field is very strong in this region, small relative errors in the precession angles that contribute to neighboring pixels translate to large absolute errors (due to the large number of precessions). Consequently, the beam polarization received by neighboring pixels varies greatly and the image appears pixilated. If infinitesimally small voxels were used instead then the variation across this region would appear smooth.

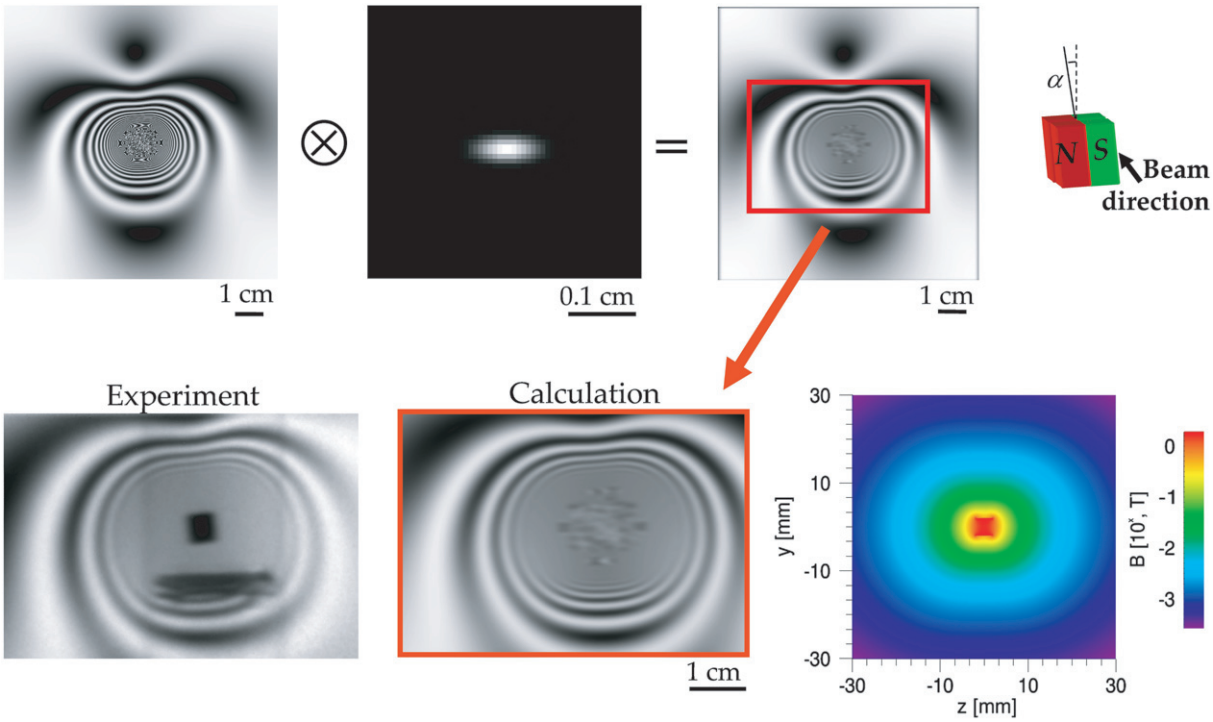

Figure 15. Experimentally measured and calculated radiographs of the magnetic field surrounding a small dipole magnet levitating above a superconducting YBCO pellet. The calculated data are convolved with a blur function (top) to approximate the resolution of the experimentally measured image (bottom). The bottom right image shows the calculated field strength for a cross section through the magnet (same orientation as in the radiographs). ([20], supplementary information.)

10. Outlook/summary

Spin-polarized neutron imaging is a non-destructive technique that allows the imaging of magnetic field distributions both in free space and within the bulk of massive samples. It is also easily adaptable to very different experimental environments (e.g. for low- or high-temperature investigations) and samples can be investigated from almost any viewing angle, revealing 3D information about the field distribution. In simple cases, 1D spin analyses can enable tomographic reconstruction of 3D magnetic fields.

However, the method is still being developed and requires some refinement in order to extend its applicability to any given magnetic system. Before this can be realized there are two key areas that require attention.

Firstly, the experimental equipment and setup must be redesigned in order to improve the attainable spatial resolution; in particular, the sample–detector distance must be reduced. Standard neutron radiography can currently achieve $\sim$50 μm spatial resolution, whereas spin-polarized neutron radiography can currently only achieve $\sim$500 μm; in any imaging application, spatial resolution is often a critical factor.

Secondly, and more importantly, is the conception of new algorithms that allow the translation of projections recorded at different viewing angles into 3D magnetic vector field matrices.

Future applications of spin-polarized neutron imaging will include further investigations of many effects in bulk magnetism. The most important of these could be magnetic domain distributions in crystals, and magnetoelastic and magnetostrictive stress and strains.

References

[1] Lehmann E and Kardjilov N 2008 *Advanced Tomographic Methods in Materials Research and Engineering* ed J Banhart (New York: Oxford University Press) pp 375–406

[2] Herman G T 1980 *Image Reconstruction from Projections: The Fundamentals of Computerized Tomography* (New York: Academic)

[3] Schillinger B, Lehmann E and Vontobel P 2000 3D neutron computed tomography: requirements and applications *Physica* B **276** 59–62

[4] Kardjilov N, Hilger A, Manke I, Strobl M and Banhart J 2005 Industrial applications at the new cold neutron radiography and tomography facility of the HMI *Nucl. Instrum. Methods* A **542** 16–21

[5] Allman B E, McMahon P J, Nugent K A, Paganin D, Jacobson D L, Arif M and Werner S A 2000 Phase radiography with neutrons *Nature* **408** 158–9

[6] Pfeiffer F, Grünzweig C, Bunk O, Frei G, Lehmann E and David C 2006 Neutron phase imaging and tomography *Phys. Rev. Lett.* **96** 215505

[7] Manke I, Hartnig Ch, Grünerbel M, Kaczerowski J, Lehnert W, Kardjilov N, Hilger A, Banhart J, Treimer W and Strobl M 2007 Quasi-*in situ* neutron tomography on polymer electrolyte membrane fuel cell stacks *Appl. Phys. Lett.* **90** 184101

[8] Strobl M, Grünzweig C, Hilger A, Manke I, Kardjilov N, David C and Pfeiffer F 2008 Neutron dark-field tomography *Phys. Rev. Lett.* **101** 123902

[9] Hickner M A, Siegel N P, Chen K S, Hussey D S, Jacobson D L and Arif M 2008 *In situ* high-resolution neutron radiography of cross-sectional liquid water profiles in proton exchange membrane fuel cells *J. Electrochem. Soc.* **155** B427–34

[10] Boillat P, Kramer D, Seyfang B C, Frei G, Lehmann E, Scherer G G, Wokaun A, Ichikawa Y, Tasaki Y and Shinohara K 2008 *In situ* observation of the water distribution across a PEFC using high resultion neutron radiography *Electrochem. Commun.* **10** 546–50

[11] Manke I, Hartnig Ch, Kardjilov N, Messerschmidt M, Hilger A, Strobl M, Lehnert W and Banhart J 2008 Characterization of water exchange and two-phase flow in porous gas diffusion materials by hydrogen–deuterium contrast neutron radiography *Appl. Phys. Lett.* **92** 244101

[12] Ankner J F and Felcher G P 1999 Polarized-neutron reflectometry *J. Magn. Magn. Mater.* **200** 741–54

[13] Gammel P and Bishop D 1998 Fingerprinting vortices with smoke *Science* **279** 410–1

[14] Jooss Ch, Albrecht J, Kuhn H, Leonhardt S and Kronmüller H 2002 Magneto-optical studies of current distributions in high-T_c superconductors *Rep. Prog. Phys.* **65** 651–788

[15] Johansen T H and Shantsev D V 2004 *Magneto-Optical Imaging* (Dordrecht: Springer)

[16] Mezei F 1972 Neutron spin echo: a new concept in polarized thermal neutron techniques *Z. Phys.* **255** 146–60

[17] Brandstätter G, Weber H W, Chattopadhyay T, Cubitt R, Fischer H, Wylie M, Emel'chenko G A and Wiedenmann A 1997 Neutron diffraction by the flux line lattice in $YBa_2Cu_3O_{7-\delta}$ single crystals *J. Appl. Crystallogr.* **30** 571–4

[18] Schlenker M, Bauspiess W, Graeff W, Bonse U and Rauch H 1980 Imaging of feromagnitic domains by neutron interferometry *J. Magn. Magn. Mater.* **15–18** 1507–9

[19] Rauch H and Werner S 2000 *Neutron Interferometry* (Oxford: Oxford University Press)

[20] Kardjilov N, Manke I, Strobl M, Hilger A, Treimer W, Meissner M, Krist T and Banhart J 2008 Three-dimensional imaging of magnetic field with polarized neutrons *Nat. Phys.* **4** 399–403

[21] Kardjilov N, Manke I, Hilger A, Dawson M and Banhart J 2008 Tech spotlight: imaging with magnetic neutrons *Adv. Mater. Process.* **166** 43–4
[22] Manke I, Kardjilov N, Strobl M, Hilger A and Banhart J 2008 Investigation of the skin effect in the bulk of electrical conductors with spin-polarized neutron radiography *J. Appl. Phys.* **104** 076109
[23] Strobl M, Treimer W, Walter P, Keil S and Manke I 2007 Magnetic field induced differential neutron phase contrast imaging *Appl. Phys. Lett.* **91** 254104
[24] Mezei F (ed) 1980 *Neutron Spin Echo Lecture Notes in Physics* vol 128 (Berlin: Springer)
[25] Hilger A, Kardjilov N, Strobl M, Treimer W and Banhart J 2006 The new cold neutron radiography and tomography instrument CONRAD at HMI Berlin *Physica* B **385–386** 1213–5
[26] Treimer W, Strobl M, Kardjilov N, Hilger A and Manke I 2006 Wavelength tunable device for neutron radiography and tomography *Appl. Phys. Lett.* **89** 203504
[27] Krist T, Kennedy S J, Hick T J and Mezei F 1998 New compact neutron polarizer *Physica* B **241–243** 82–5
[28] Krist T, Peters J, Shimizu H M, Suzuki J and Oku T 2005 Transmission bender for polarizing neutrons *Physica* B **356** 197–200
[29] Piegsa F M, van den Brandt B, Hautle P and Konter J A 2008 Neutron spin phase imaging *Nucl. Instrum. Methods* A **586** 15–7
[30] Banhart J (ed) 2008 *Advanced Tomographic Methods in Materials Research and Engineering* (Oxford: Oxford University Press)
[31] Hochhold M, Leeb H and Badurek G 1996 Tensorial neutron tomography: a first approach *J. Magn. Magn. Mater.* **157–158** 575–6
[32] Badurek G, Hochhold M and Leeb H 1997 Neutron magnetic tomography—a novel technique *Physica* B **234–236** 1171–3
[33] Badurek G, Hochhold M, Leeb H, Buchelt R and Korinek F 1997 A proposal to visualize magnetic domains within bulk materials *Physica* B **241–243** 1207–9
[34] Leeb H, Hochhold M, Badurek G, Buchelt R J and Schricker A 1998 Neutron magnetic tomography: a feasibility study *Aust. J. Phys.* **51** 401–13
[35] Leeb H, Szeywerth R, Jericha E and Badurek G 2005 Towards manageable magnetic field retrieval in bulk materials *Physica* B **356** 187–91
[36] Jericha E, Szeywerth R, Leeb H and Badurek G 2007 Reconstruction techniques for tensorial neutron tomography *Physica* B **397** 159–61
[37] Herman G T 1980 *Image Reconstruction from Projections: The Fundamentals of Computerized Tomography* (New York: Academic)